Case Study

Geothermal Energy Extraction–Induced Ground Movement Monitoring by InSAR and Its Implication for Reservoir Management

Zhaoxi Wang, Ph.D.[1]; Boshun Lv[2]; Jonathan Li, Ph.D.[3]; and Shunde Yin, Ph.D., P.Eng., F.ASCE[4]

Abstract: Global climate change highlights the significance of renewable clean energy. Geothermal energy from oilfields is abundant and can be utilized for residential heating and oil transportation. However, unreasonable heat exchange methods lead to groundwater level decline. Differences and delays between water extraction and reinjection inevitably cause land subsidence, hindering the sustainable utilization of geothermal energy resources. It is crucial to effectively monitor large-scale ground surface deformation characteristics in geothermal fields. In the research, 55 Sentinel-1A images from October 2018 to May 2022 were collected, and the ground deformation of Caofeidian new district in Bohai Bay Basin, where Nanpu Oilfield is located, in North China, was inverted by short baseline subsets-interferometric synthetic aperture radar (SBAS-InSAR) technology. The maximum subsidence velocity in Caofeidian new district exceeded 50 mm/year. Since April 2019, there has been concentrated ground subsidence in the Caofeidian new district, with a maximum cumulative subsidence exceeding 50 mm. The maximum cumulative subsidence exceeded 150 mm by May 2022. Combined with pumping and recharging tests near heating project in Caofeidian new district, the temporal subsidence mechanisms were revealed. The water extraction from the thermal reservoir caused drainage consolidation of the strata, triggering rapid subsidence in November. In April, discrepancy between water extraction and reinjection flow rate in thermal reservoir caused drainage consolidation of the strata, further exacerbating the subsidence trend. During rainy seasons, despite water reinjection and groundwater replenishment from precipitation, the strata in the Caofeidian new district underwent irreversible plastic deformation, with a slow rebound process, lagging behind urban areas without geothermal development by one month. InSAR is a reliable technology for understanding the ground deformation process in geothermal fields. Clarifying the subsidence mechanisms guides the selection of water-heat exchange methods, ensuring the sustainable development of geothermal resources. **DOI: 10.1061/JLEED9.EYENG-5523.**

Author keywords: Renewable energy; Geothermal energy engineering; Ground surface deformation; Remote sensing; InSAR; Ground control; Reservoir management.

Introduction

Entering the industrial era, with the increase in population and living standards, the global consumption of fossil fuels has sharply risen. Currently, approximately 85 million barrels of oil (about 12 million tons), 8 billion cubic meters of natural gas, and 16 million tons of coal are consumed daily (Olah et al. 2011). However, fossil fuel reserves are limited, unevenly distributed, and the renewable time for fossil energy is in the millions of years. The available resources for oil and natural gas are expected to last only until the end of this century (Pirjola et al. 2019; Wang et al. 2020). Furthermore, the combustion and oxidation process of fossil fuels and their products accelerate the global carbon cycle, leading directly to the issue of global warming as carbon dioxide rapidly increases in the atmosphere (Hoang and Pham 2021). The societal demand for renewable alternative energy sources, such as hydro, geothermal, solar, wind, nuclear energy, is becoming increasingly intense (Pirjola et al. 2019; Wang et al. 2020). Reshaping the energy landscape is a crucial breakthrough for achieving sustainable development in industrial society (Hoang and Pham 2021; Nadeem et al. 2023).

The unified mantle background, similar geological conditions, and favorable reservoir-seal combinations in rift basins provide conditions for the co-storage of oil and gas resources with geothermal resources (Aydin and Merey 2021; Majorowicz and Moore 2014). Geothermal energy, as a green, low-carbon, and recyclable clean energy source, possesses characteristics such as large reserves, widespread distribution, and high stability. With the ongoing depletion of oil and gas resources, geothermal energy has become a crucial component in the diversified development of oil, gas, and heat resources. The geological data accumulated during oil and gas exploration lay the foundation for efficient and large-scale utilization of geothermal resources (Aydin and Merey 2021; Majorowicz and Moore 2014). Simultaneously, the thermal energy generated during oil and gas well exploitation can be used for residential heating and oil transportation. Additionally, the reuse of abandoned

[1]Visiting Ph.D. Candidate, Dept. of Civil and Environmental Engineering, Univ. of Waterloo, Waterloo, ON, Canada, N2L 3G1; Ph.D. Candidate, College of Construction Engineering, Jilin Univ., Changchun, Jilin 130026, PR China. ORCID: https://orcid.org/0009-0003-5389-5004. Email: zhaoxiw22@mails.jlu.edu.cn

[2]President, Jidong Oilfield Renewable Energy Company of PetroChina, Tangshan, Hebei 063004, PR China. Email: jd_lbs@petrochina.com.cn

[3]Professor, Dept. of Geography and Environmental Management, Univ. of Waterloo, Waterloo, ON, Canada, N2L 3G1. Email: junli@uwaterloo.ca

[4]Professor, Dept. of Civil and Environmental Engineering, Univ. of Waterloo, Waterloo, ON, Canada, N2L 3G1 (corresponding author). Email: shunde.yin@uwaterloo.ca

Note. This manuscript was submitted on February 19, 2024; approved on May 9, 2024; published online on August 1, 2024. Discussion period open until January 1, 2025; separate discussions must be submitted for individual papers. This paper is part of the ***Journal of Energy Engineering***, © ASCE, ISSN 0733-9402.

oil wells saves production costs and facilitates the technological and product transformation in traditional oilfields.

In the development of geothermal energy, the key lies in sophisticated reservoir management and rational heat exchange from the thermal fluid. Shortsighted methods, including only extraction without replenishment and disorderly extraction and discharge, lead to a decline in the groundwater level. The decline triggers severe ground subsidence issues and results in extremely low efficiency in geothermal field development (Cigna et al. 2019). In recent years, the extract heat without extracting water model, based on balanced production and reinjection technology, has been applied. However, for porous thermal reservoirs, factors such as physical blockages, the clogging effect of organic substances in reinjected water, and blockages caused by the heat source would lead to differences and delays between pumping and reinjection volumes. Changes in the volume and pressure of geothermal fluids have led to subsidence and even collapse of the ground in geothermal fields, impacting their sustainable development (García-Gil et al. 2016). In the context of large-scale extraction of oil, gas, and geothermal energy in coastal oilfields, the continuous decline in groundwater level can trigger seawater intrusion issues, threatening to the inland hydrogeological environment. It severely restricts agricultural production and regional development. Therefore, monitoring ground subsidence caused by geothermal field development and assessing the potential impacts of geothermal energy extraction on the geological environment are crucial issues for the rational utilization of geothermal resources. It can provide essential information for the planning and operation of geothermal fields.

Due to the great depth of geothermal reservoirs, the challenges of high pressure and high-temperature environments for sensors are considerable (Liu et al. 2018). The process of monitoring changes in geothermal fluids is difficult, and quantifying underground deformations caused by geothermal extraction is challenging, which impedes efficient reservoir management. Therefore, it is necessary to measure ground surface deformations above the reservoir to infer the dynamics of the geothermal field, as well as the reinjection and production processes, indirectly quantifying regional ground subsidence caused by hydrothermal extraction (Hu et al. 2016; Maghsoudi et al. 2018).

Traditional ground measurement techniques, such as leveling and global navigation satellite system (GNSS), can only form low dense survey network (Cao et al. 2022a; Qin et al. 2017). Interferometric synthetic aperture radar (InSAR) technology based on satellite imagery exhibits advantages such as large-scale, low-cost, and all-weather imaging (Janna et al. 2012; Yu et al. 2020a). Therefore, InSAR technology has been widely applied to geological resource development and geological disasters associated with large-scale and hard-to-access deformations. In terms of geological resources, it can monitor phenomena such as coal fires (Jiang et al. 2011; Karanam et al. 2021), underground oil and gas activities (Fibbi et al. 2023; Liu et al. 2016; Qu et al. 2015), and excessive groundwater extraction (Chaussard et al. 2014; Hoffmann et al. 2003). InSAR technology can also be used to assess underground structural activity risks caused by activities such as CO_2 geological storage and water injection (Verdon et al. 2013; Yang et al. 2015). Additionally, the technology can invert the historical deformation modes of geological disasters such as landslides and debris flows, thereby further exploring the deformation mechanisms of these disasters (Singleton et al. 2014; Yi et al. 2022).

Some scholars have attempted to use short baseline subsets InSAR (SBAS-InSAR) to monitor long-term regional deformations caused by geothermal field development (Cigna et al. 2019; Hu et al. 2016; Liu et al. 2018; Maghsoudi et al. 2018), exploring the correlation between dynamic changes in geothermal fluids and ground deformations. SBAS-InSAR leverages SAR images within different small baseline subsets. The singular value decomposition (SVD) method can address rank deficit problems in solving interferogram phases. SBAS effectively increases the spatiotemporal sampling rate and mitigates baseline decorrelation phenomena (Berardino et al. 2002). SBAS contributes to improving the accuracy of interferometric phases acquisition (Tizzani et al. 2007), ensures the reliability of deformation monitoring, and meets the requirements for monitoring long-term ground deformations in geothermal fields.

This study, focuses on the geothermal development area in Caofeidian District located in the Bohai Bay of North China, with 55 Sentinel-1A images collected from October 2018 to May 2022, aiming at taking advantage of InSAR ground monitoring for enhanced geothermal reservoir management. First, utilizing the SBAS-InSAR technique, ground surface deformation information for the Caofeidian District were inverted, identifying two subsidence centers: Nanpu development zone and Caofeidian new district. Then, through a comparative analysis of the deformation values and the deformation time series in the subsidence centers during the heating period and rainy seasons, considering development patterns in the study area, the research revealed the subsidence mechanism of porous geothermal reservoirs. Finally, the study demonstrated the correlation between InSAR monitoring and geothermal operations, providing an effective low-cost strategy for ground control and reservoir management.

Geologic Settings of Geothermal Energy Development in Caofeidian District, Tangshan, China

Tectonic and Lithology Geological Settings

The studied geothermal field is based in Caofeidian District, Tangshan City, Hebei Province, China, which is located in the Bohai Bay Basin. The Bohai Bay Basin spans the regions of Beijing, Tianjin, Hebei, Shandong, Liaoning, and the Bohai Sea area in North China, with an area of 2×10^5 km^2 [Fig. 1(a)]. The Nanpu Sag in the Bohai Bay is located in the south-eastern direction of Tangshan City, Hebei Province [Fig. 1(b)]. Tangshan City has a north-high and south-low topography, with elevations ranging from 0 to about 800 m [Figs. 1(a and b)].

The Neogene and Quaternary subsidence periods in the Nanpu Sag witnessed frequent tectonic activities (Li and Li 2023; Li 2013) [Fig. 1(b)]. Simultaneously, the deposition of Neogene Guantao formation, Minghuazhen formation, and Quaternary strata occurred (Wei 2006; Li 2020, 2013). The thickness variation of the Guantao and Minghuazhen formations is significant, with a characteristic of thinning to the south and thickening to the north (Li 2020, 2013). The average thickness of the Guantao formation is 300–900 m, with an accumulated geothermal thickness of 120–300 m. The Minghuazhen Formation has an average thickness of 740–2000 m (Dong et al. 2021; Li 2013). The quaternary strata mainly comprise sedimentary layers of alluvial plains, showing regional unconformity contact with the underlying Neogene strata. The lithology is primarily sand and clay [Fig. 2(a)], with an average thickness of 0–300 m (Li and Li 2023; Li 2013). The present-day geothermal heat flow in the Nanpu Sag ranges from 93.8 to 100.1 mW/m^2 (Dong et al. 2021). The Jidong Nanpu Oilfield, located in the southeastern coastal area of Tangshan City within Caofeidian, produces approximately 10 million tons of oil annually and is a world-class high-yield oilfield.

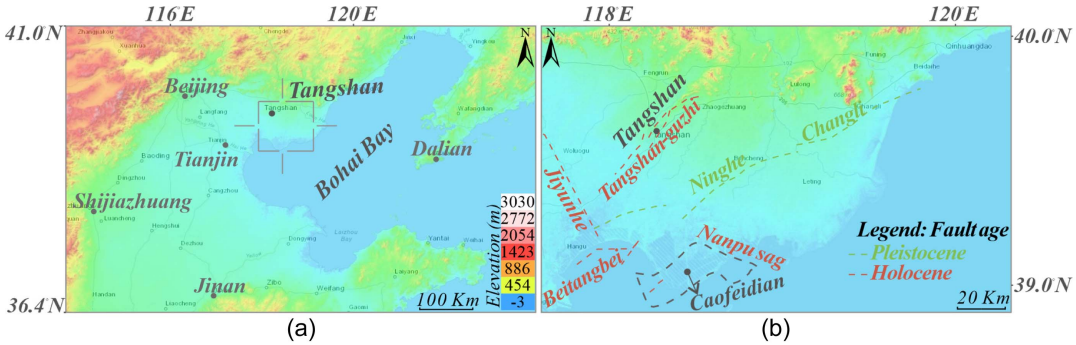

Fig. 1. Geographical location of the study area: (a) topography of Bohai Bay Basin; and (b) quaternary fault activity of Tangshan City. (Sources: Esri, HERE, Garmin, FAO, NOAA, USGS, © OpenStreetMap contributors, and the GIS User Community.)

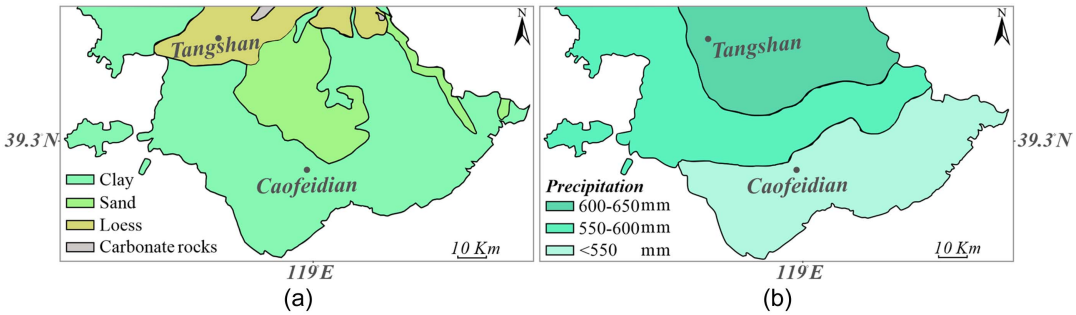

Fig. 2. (a) Regional lithology map of Tangshan City; and (b) regional precipitation map of Tangshan City. (Modified from Wei 2006.)

Climatic Setting

Tangshan City experiences a temperate continental monsoon climate with distinct seasons, concentrated rainfall from June to September. There is significant regional variation in the annual average precipitation, generally decreasing from north to south. Caofeidian District has an annual average precipitation of less than 550 mm [Fig. 2(b)] (Wei 2006). The annual average temperature in the study area ranges from 10 to 11°C, with a maximum temperature of 40°C and a minimum temperature of −28°C (Li and Li 2023).

Hydrogeological Setting

The aquifers in the study area comprise carbonate rock fracture-karst aquifers and quaternary loose porous aquifers (Wei 2006). Carbonate rock fracture-karst aquifers are distributed in the northern mountainous areas and urban areas of Tangshan, mainly consisting of Ordovician karst water (Li and Li 2023). Quaternary loose porous aquifers are found on both sides of river valleys and in the alluvial plain areas, with the groundwater level depth of the quaternary aquifer in Caofeidian District exceeding 20 m (Dong et al. 2016).

Methodology

SAR Data Set

The Sentinel satellites are members of the Copernicus program in European Space Agency. The Sentinel-1 satellites operate in the C-band and collect radar images of the Earth's surface. The Sentinel satellites possess excellent spatial coverage and revisit capabilities, with data being openly accessible. 55 SAR images from the Sentinel-1A satellite covering the Tangshan City were acquired. The images span the period from 25 October 2018 to 25 May 2022, with a time interval of 24 days. The images were obtained from frame 124 in the ascending orbit. When focusing on large-scale ground deformation patterns, neglecting horizontal surface deformation in contributing to LOS deformation, a single geometry is sufficient to acquire vertical ground deformation (Li and Li 2023; Yu et al. 2020a). Additionally, a 30 m resolution DEM mapped by the shuttle radar topography mission (SRTM) conducted by the National Aeronautics and Space Administration (NASA) was used for image registration and removal of topographic phase. The key parameters for the SAR images are summarized in Table 1.

SBAS-InSAR Processing

The SBAS-InSAR processing was conducted using the SARscape module in ENVI software. The key algorithm of SBAS-InSAR is shown in Fig. 3(a). Initially, using the image from 22 July 2020, as the reference image, 249 pairs of interferograms were generated, with the temporal baseline limited to 150 days [Fig. 3(b)].

Table 1. Key parameters for the collected SAR images

Sentinel-1A image parameter	Value
Beam mode	IW
Path	69
Frame	124
Flight direction	Ascending
Polarization	VV
Incidence angle	39.11°
Resolution	5 × 20 m

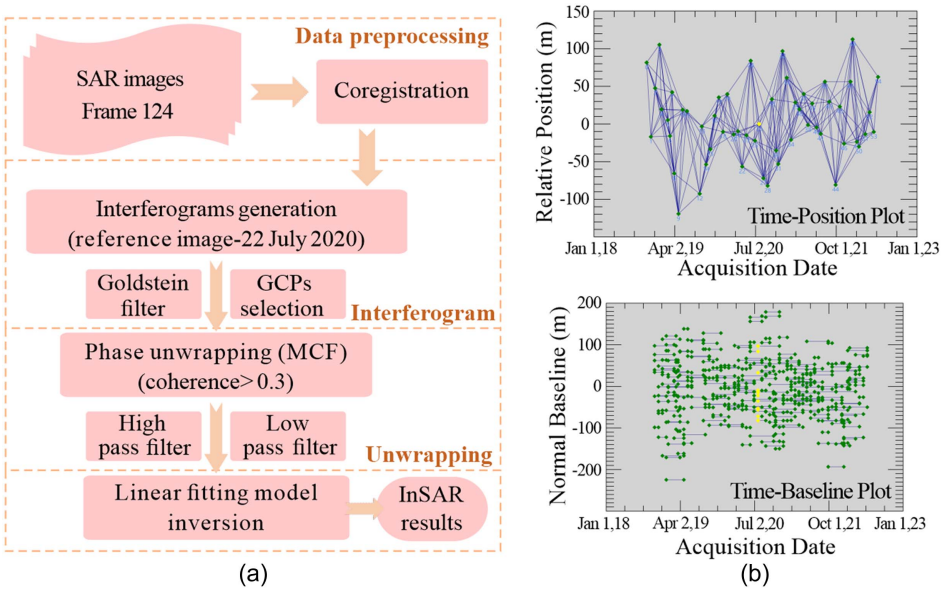

Fig. 3. (a) Key algorithm of SBAS-InSAR; and (b) spatiotemporal baseline maps.

The coherence maps of typical interferometric images for the study area were obtained (Fig. 4), along with histograms of the coherence maps (Fig. 5). During the winter seasons [Figs. 4(a-b, d, f, and h)], the interference quality in the study area was good, with an average coherence coefficient exceeding 0.4 [Figs. 5(a-b, d, f, and h)]. Particularly, coherence was notably high in the four urban areas, namely the Caofeidian district in the north, the Caofeidian industrial zone in the south, the Caofeidian new district in the east, and the Nanpu development zone in the west [Figs. 4(a-b, d, f, and h)]. In the rainy seasons [Figs. 4(c, e, g, and i)], the interference quality in the central farmland and coastal areas was relatively poor, while the interference quality in urban areas remained good. The average coherence coefficient still exceeded 0.3 [Figs. 5(c, e, g, and i)]. Subsequently, the Goldstein filtering method (Goldstein and Werner 1998; Suo et al. 2016) was employed to eliminate noise phases. 60 ground control points (GCPs) were selected to remove flat ground phase and refine the orbit (Cao et al. 2022b; Wang et al. 2023). The minimum cost flow algorithm (MCF) was applied for phase unwrapping in pixels with a coherence coefficient >0.3. A total of 39 interferogram pairs were discarded based on the interferometric quality and unwrapping effectiveness. Finally, atmospheric phases were filtered using high pass filtering and low pass filtering methods, and a robust linear fitting model (Wang et al. 2023; Wang et al. 2024) (https://www.sarmap.ch/tutorials/SBAS_Tutorial_562.pdf) was employed to invert ground deformation velocity. The deformation results were then transformed from radar coordinates to the line-of-sight (LOS) direction (d_{LOS}), and the vertical deformation velocity (d_v) was further determined according to the satellite incidence angle (θ) utilizing the formula (Li and Li 2023; Yu et al. 2020a):

$$d_v = -\frac{d_{LOS}}{\cos\theta} \tag{1}$$

Correlation between Site Deformation Characteristics and Reservoir Management

In the process of geothermal oilfield production, parameters such as temperature and pressure of the fluids within the reservoir undergo changes. These variations in the fluid field lead to alterations in the stress and strain fields of the reservoir matrix, manifested macroscopically as deformation of the reservoir site. It is challenging to deploy sensors to monitor the activities within the reservoir in high-temperature and high-pressure environments. Geertsma (1966, 1973) derived the relationship between vertical deformation of the reservoir center (u_z) and internal pressure drop (Δ_p) based on Biot consolidation theory

$$u_z = -2(1-\upsilon)c_m\alpha h\Delta_p\left(1-\frac{B}{\sqrt{1+B^2}}\right),$$
$$c_m = \frac{(1+\upsilon)(1-2\upsilon)}{E(1-\upsilon)}, \qquad B = \frac{C}{R} \tag{2}$$

where υ = Poisson's ratio of the reservoir matrix, E = elastic module of the reservoir matrix, α = Biot-Willis coefficient, h = reservoir thickness, C = buried depth of the reservoir center, and R = radius of the reservoir.

Therefore, by using InSAR to acquire large-scale deformation characteristics of the site, it is possible to infer the changes in pressure and stress within the reservoir. Particularly, under different development patterns such as urban areas and geothermal oilfield development zones, InSAR can be utilized to horizontally compare the temporal deformation characteristics of different sites. Additionally, it can help identify the predominant factors driving site deformation.

Results and Analyses

Regional Deformation Characteristics

The Sentinel-1A SAR images captured between 25 October 2018 to 25 May 2022 were processed by SBAS-InSAR method. The ground deformation velocity of the Caofeidian District was inverted [Fig. 6(a)]. The maximum subsidence deformation velocity for the Caofeidian District was −94 mm/a, and the maximum uplift deformation velocity was 40 mm/a. The ground deformation in Caofeidian District exhibited four distinct deformation regions, corresponding to the four urban areas with high interference quality. The northern part of Caofeidian (region A) and the southern

Fig. 4. Coherence maps of typical interferometric images across seasons: (a–b), (d), (f), and (h) winter seasons; (c), (e), (g), and (i) rainy seasons.

Caofeidian industrial zone (region D) primarily experienced uplift, with an uplift velocity of up to 10 mm/a. In the western Nanpu development zone (region B) and eastern Caofeidian new district (region C), there was concentrated subsidence deformation, with some areas experiencing a subsidence velocity of up to −70 mm/a.

The error of InSAR deformation velocity results is shown in Fig. 6(b). The formula used for the precision calculation is (https://www.sarmap.ch/tutorials/Interferometry_DEM_v570.pdf):

$$\sqrt{\frac{1-\gamma^2}{2\gamma^2}}\frac{\lambda R \sin\theta}{4\pi B} \tag{3}$$

where γ = interferometric coherence, λ = wavelength, R = slant range distance, θ = local incidence angle, and B = normal baseline. It provides an estimate of the measurement precision. The higher this value the lower the measurement precision.

Most areas in Caofeidian District demonstrated good accuracy in deformation velocity (<5.10 mm/a), with high precision in urban areas like regions B and C (0.14–1.79 mm/a), especially in the well-established and developed region A [Fig. 6(b)]. For middle farmland and coastal areas, the coherence of SAR images was compromised by water during rainy seasons [Figs. 4(c, e, g, and i)] leading to relatively low accuracy (>5.10 mm/a) [Fig. 6(b)].

Spatiotemporal Deformation Characteristics of the Local Regions

From 25 October 2018 to 25 May 2022, the cumulative ground deformation in Caofeidian District was mostly distributed in the range of −250 mm to 200 mm (Fig. 7). From October 2018 to December 2018 [Fig. 7(a)], a pale red patchy area appeared in the central part of the study area, indicating widespread slight subsidence phenomena with subsidence values within −50 mm.

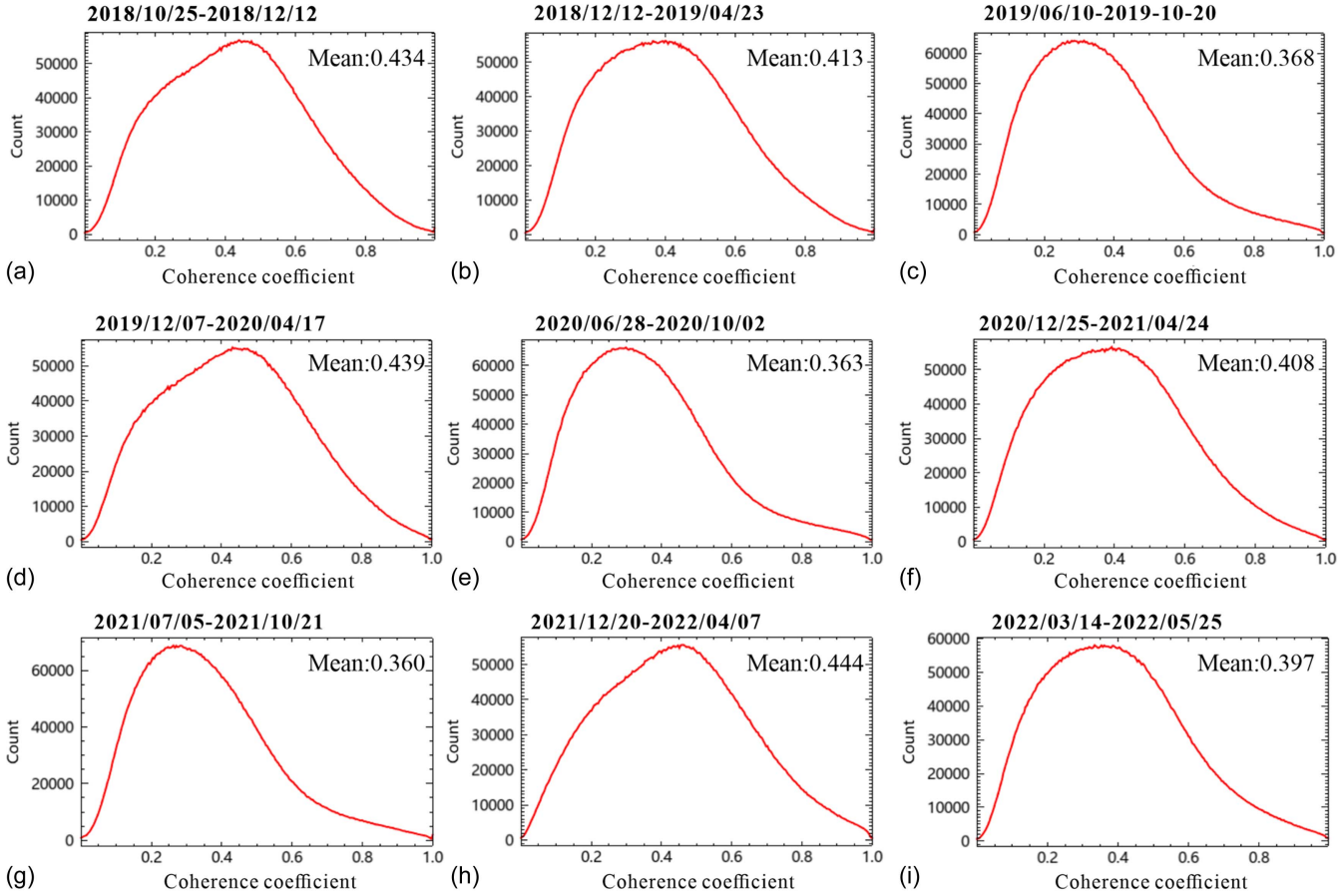

Fig. 5. Histograms of coherence maps across seasons: (a–b), (d), (f), and (h) winter seasons; (c), (e), (g), and (i) rainy seasons.

Slight subsidence occurred in regions B, C, and D, while the subsidence phenomenon was less pronounced in region A [Fig. 7(a)]. By April 2019 [Fig. 7(b)], the subsidence trend in the central region of the study area eased, with the subsidence trend disappearing in region D. Regions B and C still exhibited a subsidence trend. Additionally, a small area in the region C appeared in fiery red color, indicating localized concentrated subsidence, where subsidence values exceeded 50 mm [Fig. 7(b)]. By October 2019 [Fig. 7(c)], the subsidence trend in the central part of the study area further eased, while regions B and C still maintained a subsidence trend. By April 2020 [Fig. 7(d)], the pale red patchy area in the central part of the study area gradually disappeared, with further easing of the subsidence trend. Regions B and C still exhibited a subsidence trend [Fig. 7(d)]. Region D showed a significant uplift deformation area, where uplift values exceeded 50 mm [Fig. 7(d)]. By October 2020 [Fig. 7(e)], partial uplift deformation areas appeared in the region A, where uplift values exceeded 50 mm. By April 2021 [Fig. 7(f)], the uplift deformation areas in regions A and D further expanded, with uplift values exceeding 50 mm. The subsidence trend in regions B and C further intensified, with a significant increase in the area of fiery red areas where subsidence values exceeded 50 mm [Fig. 7(f)]. By October 2021 [Fig. 7(g)], the uplift deformation trend in regions A and D further intensified, with areas showing uplift values exceeding 100 mm. The subsidence trend in region C further intensified, with areas showing subsidence values exceeding 150 mm [Fig. 7(g)]. By May 2022 [Fig. 7(h)], the areas with uplift values exceeding 100 mm in regions A and D further increased. The subsidence trend in region C further intensified, with the area showing subsidence values exceeding 150 mm further expanding [Fig. 7(h)].

To understand the development trends of cumulative ground deformation in regions with concentrated subsidence, the time series curves of all deformation result points were averaged for regions B and C, resulting in the time series deformation curves for each region [Fig. 8(a)]. The deformation time series curves of subsidence centers B and C were locally magnified [Figs. 8(b–d)].

During the first heating season in 2018, from November 2018 to April 2019 [Fig. 8(a)], region B exhibited a sustained subsidence trend, while region C showed alternating patterns of subsidence and uplift deformation. Starting from December 2018 [Fig. 8(a)], region C initially displayed significant subsidence followed by uplift deformation, then continued subsiding. By March 2019 [Fig. 8(b)], region C experienced uplift deformation again. By the end of April 2019 [Fig. 8(b)], region C continued to undergo subsidence deformation, while the subsidence trend in region B ended, transitioning to uplift deformation. By June 2019 [Fig. 8(b)], region B shifted back to subsidence, while region C experienced uplift deformation. From September 2019 to the end of February 2020 [Fig. 8(a)], regions B and C both exhibited consistent subsidence trends. Starting from March 2020 [Fig. 8(c)], region C began to uplift, while region B continued to subside. Region C shifted back to subsidence by May 2020, with slight uplift occurring in June and September 2020 [Fig. 8(c)]. The subsidence trend in region B ended in April 2020, transitioning to uplift [Fig. 8(c)]. From October 2020 to the end of April 2021 [Fig. 8(a)], both regions B and C exhibited consistent subsidence trends. The subsidence trend in region C ended in June 2021, with uplift deformation continuing until August 2021 [Fig. 8(d)]. The subsidence trend in region B ended in late April 2021, showing uplift in May 2021 [Figs. 8(a and d)]. From September 2021 to the

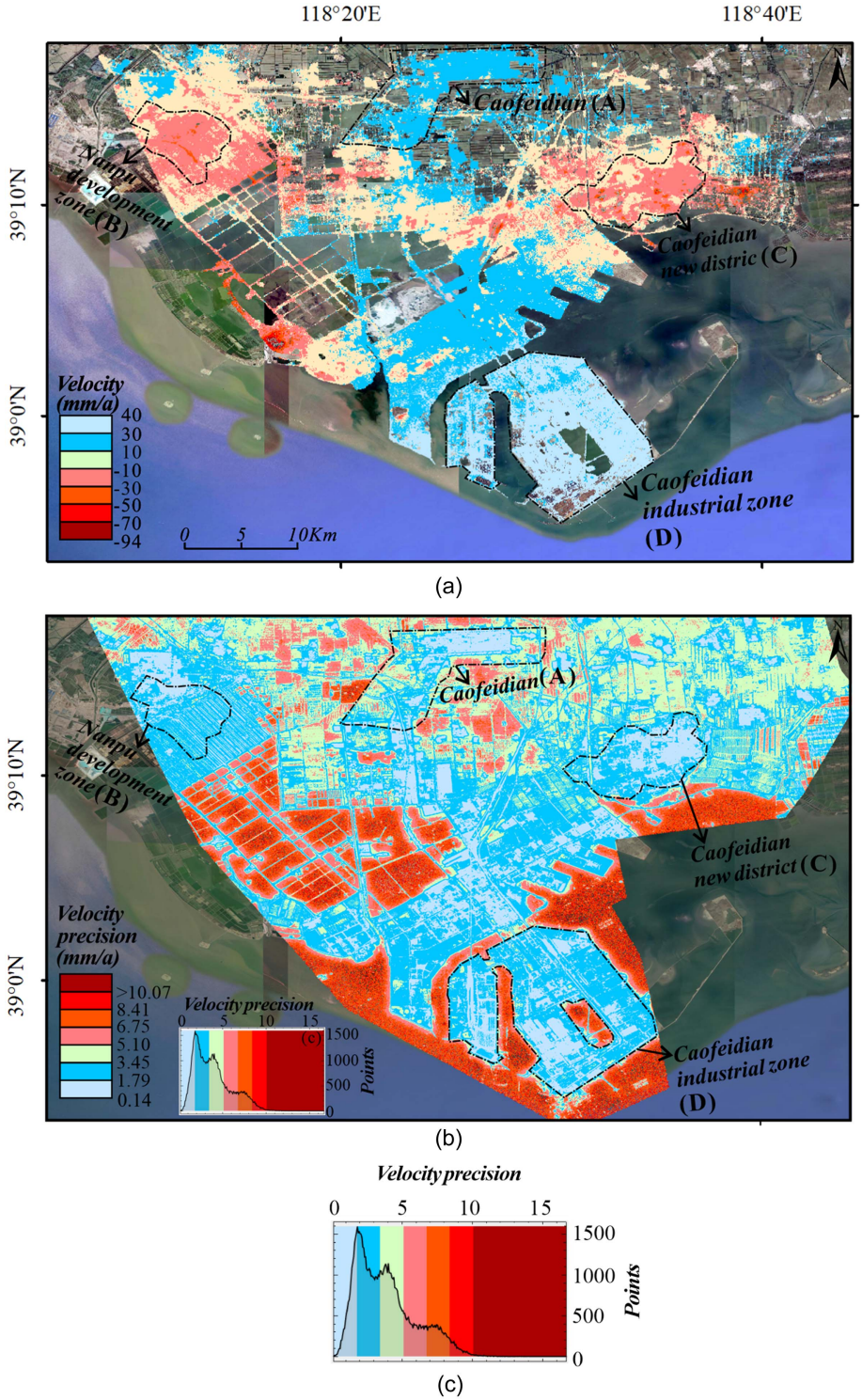

Fig. 6. SBAS-InSAR results of (a) ground deformation velocity of the Caofeidian District and (b) deformation velocity error overlaid on the satellite imagery in the Caofeidian District; and (c) counting points of deformation velocity error.

beginning of February 2022, regions B and C showed consistent subsidence trends [Fig. 8(a)]. The subsidence trend in region C ended in March 2022, with uplift deformation continuing until May 2022 [Fig. 8(a)]. The subsidence trend in region B ended in late April 2022, showing uplift in May 2022 [Fig. 8(a)].

From 2018 to 2022, the time series deformation characteristics of regions B and C exhibited certain regularities. The summary is as follows: during the heating seasons, region B maintained a continuous subsidence trend, while region C exhibited the characteristic of rapid ground subsidence followed by uplift deformation. After the heating seasons ended, in early May, there was a further intensification of the subsidence trend in region C, while the subsidence trend in region B remained relatively unchanged, even beginning to show uplift deformation. There was concentrated rainfall in Caofeidian District during June and September (Fig. 9). Upon entering the rainy season in June, the subsidence trend in region

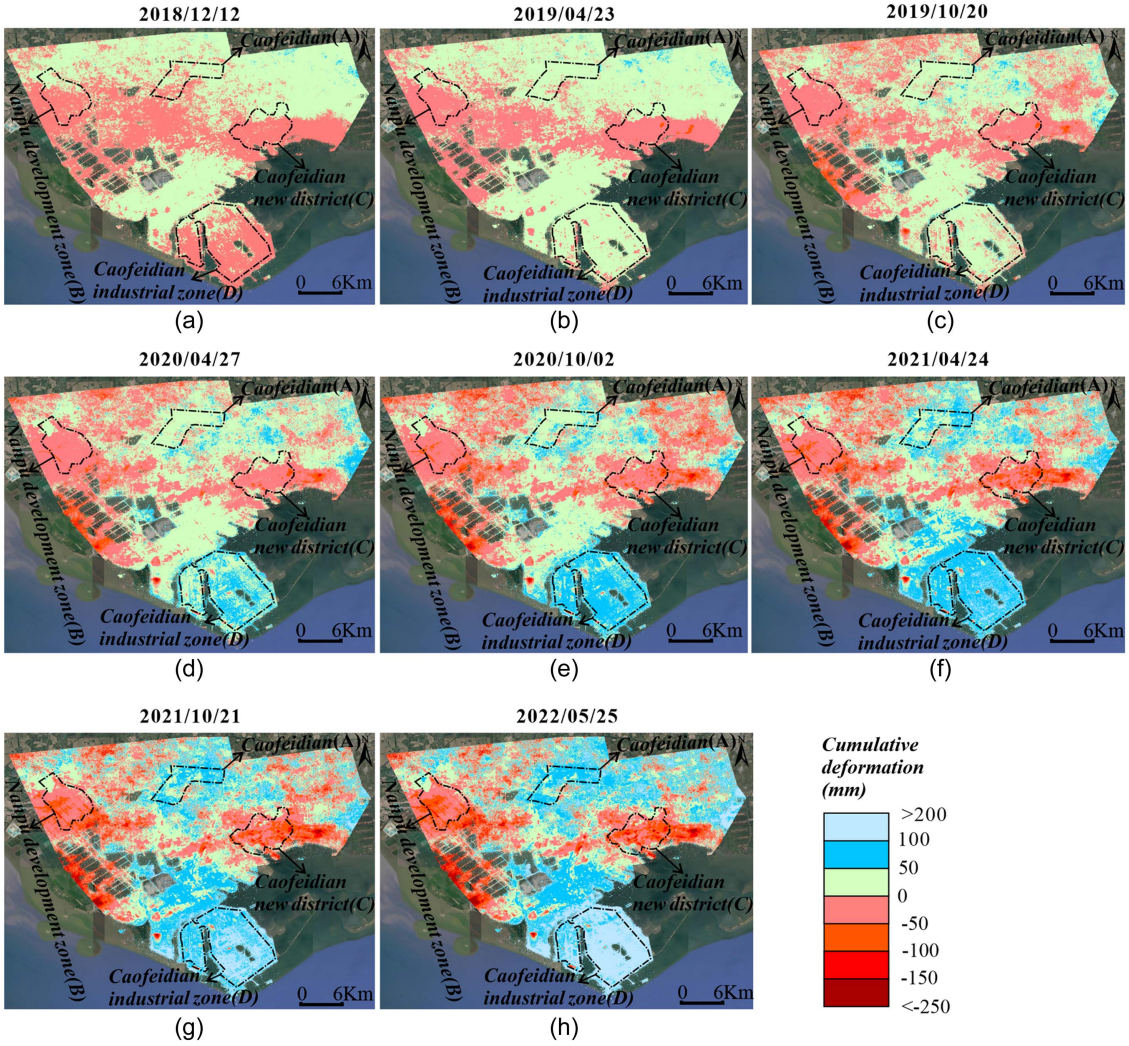

Fig. 7. Cumulative deformation of Caofeidian District in: (a) December 2018; (b) April 2019; (c) October 2019; (d) April 2020; (e) October 2020; (f) April 2021; (g) October 2021; and (h) May 2022.

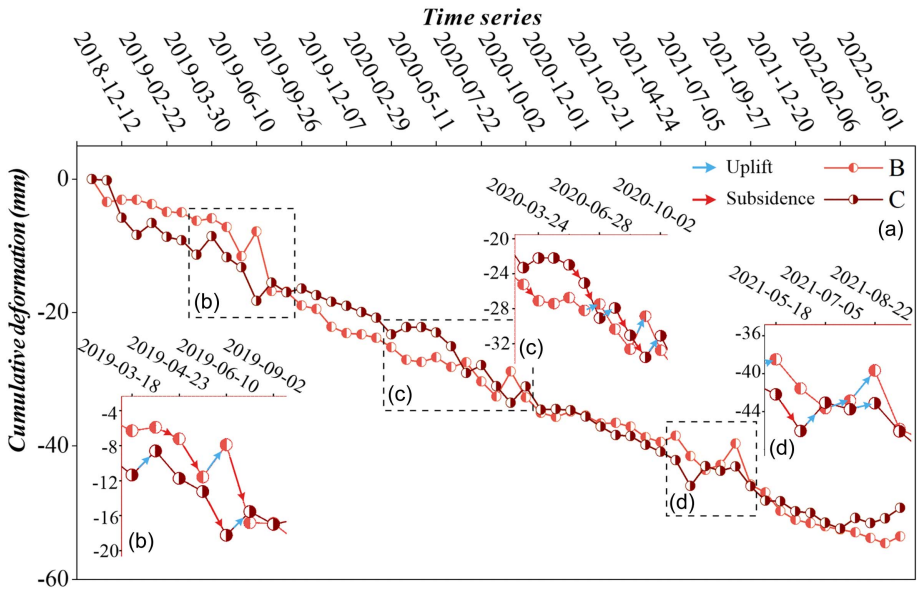

Fig. 8. (a) Time series curves of cumulative deformation in the divided regions; locally magnification in time series curves of cumulative deformation during (b) March 2019 to September 2019; (c) March 2020 to October 2020; and (d) May 2021 to August 2021.

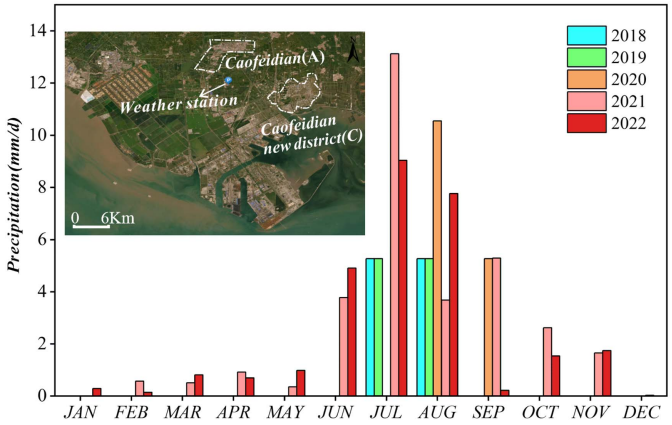

Fig. 9. Monthly average precipitation in Caofeidian District between 2018 and 2022. (Base map data source: Esri, ArcGIS Online; precipitation data source: https://power.larc.nasa.gov/.)

C was restrained, exhibiting alternating patterns of subsidence and uplift. Region B also displayed this characteristic. However, interestingly, there was a temporal gap between the transition points of subsidence and uplift in regions B and C, with region B experiencing uplift deformation earlier, approximately one month before region C. Clearly, in June 2019, September 2020, and July 2021 [Figs. 8(b–d)], region B experienced significant uplift deformation while region C still maintained a subsidence trend. One month later, region C underwent uplift deformation.

Feasibility of Monitoring Ground Surface Deformation in Geothermal Fields by InSAR

Against the backdrop of reducing global carbon emissions, finding new energy sources to replace traditional fossil fuels is a key issue for the development of industrial society. In the Nanpu Oilfield of Caofeidian in North China, the extensive accumulation in oil and gas exploration data economically facilitates the development of geothermal energy resources. Since 2018, geothermal projects have been vigorously developed in Caofeidian new district, and by the end of 2023, the geothermal heating area has reached 16.66 million m^2, saving approximately 406,800 tons of coal (Dong et al. 2021).

However, the problem of ground subsidence has also emerged with geothermal development. The study identified concentrated subsidence areas in the Caofeidian new district, where the maximum subsidence velocity exceeded 50 mm/year [Fig. 6(a)]. Since April 2019, there has been concentrated ground subsidence in the Caofeidian new district, with a maximum cumulative subsidence exceeding 50 mm [Fig. 7(d)]. By the end of May 2022, the maximum cumulative subsidence in the Caofeidian new district exceeded 150 mm [Fig. 7(h)]. Li and Li (2023) utilized Sentinel-1A data from 2019 to 2021 to obtain the spatiotemporal characteristics of ground deformation in the Caofeidian District. It was observed that the middle regions of the Caofeidian District exhibited a distinct blocklike subsidence distribution. Since May 2020, there has been concentrated ground subsidence in the Caofeidian new district. The maximum ground subsidence velocity in the Caofeidian new district exceeded 50 mm/year during the study period. The finding is consistent with the InSAR results in this study, confirming the reliability of the deformation analysis.

Geothermal Production and Water Reinjection Test

To explore the driving factors of deformation during the heating seasons in Caofeidian new district, we referenced the results of co-level water extraction and reinjection tests conducted approximately 1 km southwest of the Caofeidian new district (Dong et al. 2021). The two wells are about 250 m apart at the wellheads and 380 m apart at the bottoms, both extracting and recharging water from the Guantao Formation at depths of 2,050 to 2,150 m. Monitoring data on dynamic water levels and flow rates of the extraction and reinjection wells were obtained for the heating season in 2019-2020 [Figs. 10(a–c)]. Following the onset of the heating season in November, there was a significant increase in the thermal reservoir water extraction, leading to a rapid decline in the dynamic water level and flow rate of the extraction well [Figs. 10(a and c)]. After the heat exchange process, groundwater reinjection was carried out, causing the dynamic water level and flow rate of the reinjection well to gradually rise in December [Figs. 10(b and c)]. The groundwater flow in the extraction well was replenished, alleviating the declining trend of the dynamic water level in December and maintaining relative stability [Fig. 10(a)]. After continuous groundwater reinjection for a period, the dynamic water level and flow rate in the thermal reservoir showed a slight rise [Figs. 10(b and c)].

By February, the water extraction of the thermal reservoir was further increased, but the reinjection volume was not promptly and fully replenished into the thermal reservoir strata. It is likely due to

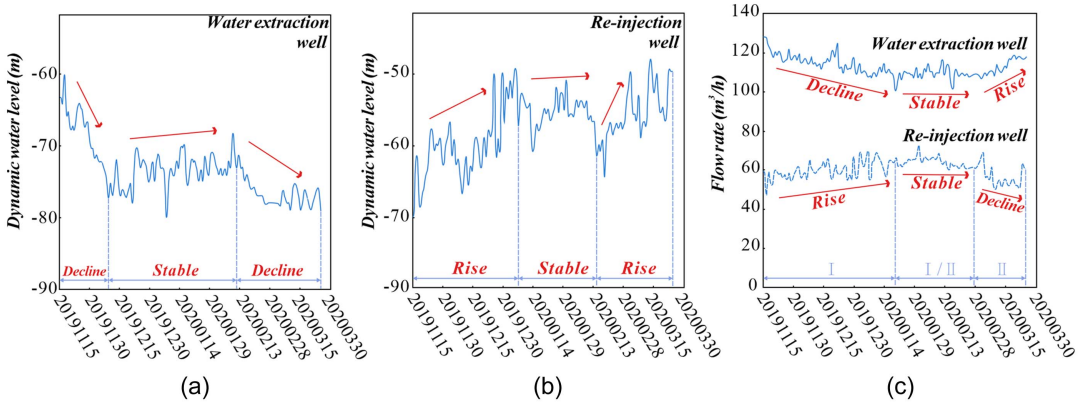

Fig. 10. Dynamic water level in (a) water extraction well and (b) reinjection well during the heating season from 2019 to 2020; (c) flow rate in water extraction well and reinjection well during the heating season from 2019 to 2020 (modified from Dong et al. 2021).

a lag in reinjection, as well as the influence of factors such as physical blockage, clogging by organic compounds in the reinjection water, and blockage caused by the heat source. As a result, there was an increased discrepancy in flow rate between the water extraction and reinjection wells [Fig. 10(c)]. The consequence was a continuous decline in the dynamic water level of the extraction well [Fig. 10(a)].

Implications for Geothermal Reservoir Management

Deformation Mechanisms of Concentrated Subsidence Regions

The geothermal system is formed by the interaction of the underground water system and geological structures (Bo et al. 2021; Wang et al. 2013). During the development of geothermal reservoirs, changes in groundwater pressure and flow can trigger site deformation (Geertsma 1957, 1966, 1973). Timely management of concentrated subsidence ensures the sustainable development of the reservoir. Based on the subsidence characteristics of the site obtained through InSAR, the driving mechanisms of groundwater system changes on subsidence can be investigated. It provides categorized guidance for urban ground control and geothermal reservoir management, facilitating rational development of geothermal fields.

The lithology in the Quaternary strata primarily comprises clay and sand, being in a state of normal consolidation or underconsolidation. In the hydrogeological context of Caofeidian District, where the groundwater level is deep (>20 m) (Dong et al. 2016), the thin weakly bound water film forms on the surface of clay minerals in soil, and the drainage conditions in clay soil are good (Yu et al. 2020b). It is also important to note that newly developed urban areas have a strong demand for groundwater, and the extraction of groundwater for daily life further accelerates the consolidation subsidence process in the quaternary strata (Li and Li 2023; Liu et al. 2003; Shen et al. 2014).

InSAR generated deformation time series for the subsidence centers (Fig. 8), offering valuable historical data to analyze the predominant factors influencing regional subsidence under different development patterns. Through comparative analysis of deformation characteristics during the heating seasons and rainy seasons, the subsidence mechanisms of the Nanpu development zone and Caofeidian new district can be summarized. During the heating seasons, Nanpu development zone consistently maintained a subsidence trend (Fig. 8). However, Caofeidian new district exhibited a temporal deformation pattern characterized by rapid subsidence in the initial stage (Stage I), followed by alternating uplift and subsidence in subsequent stage (Stage II) (Fig. 11). Under similar climatic conditions, strata properties, and urbanization development patterns, the differences of the temporal deformation characteristics in these two regions were likely influenced by fluctuations in

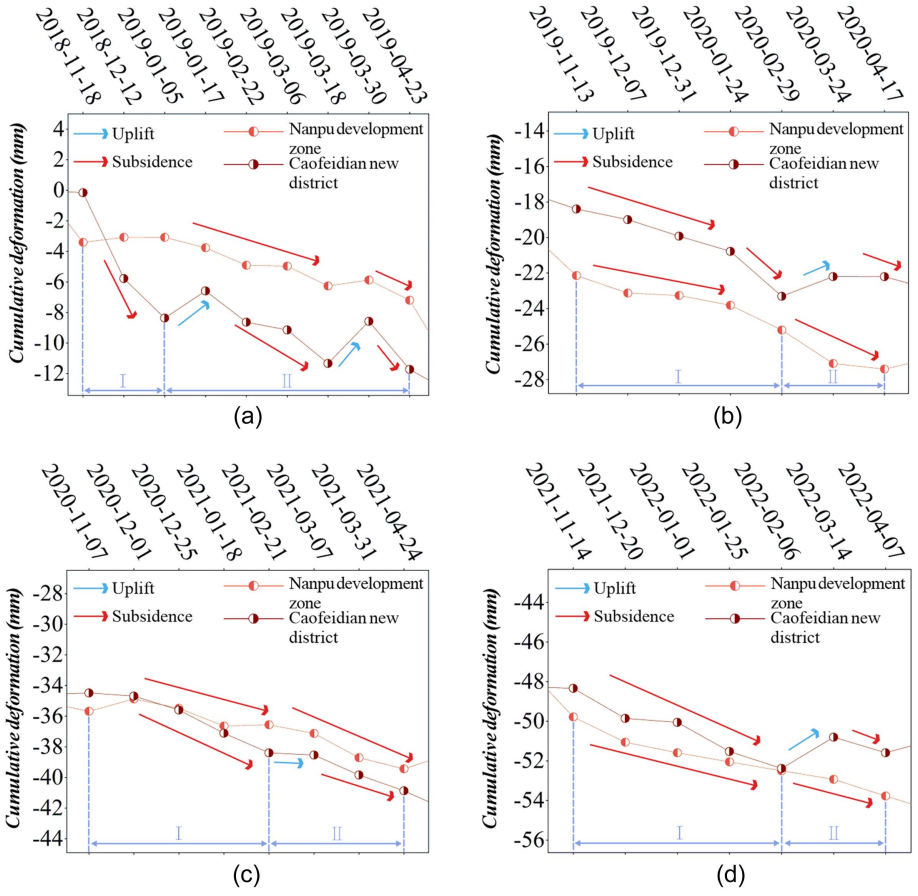

Fig. 11. Time series curves of cumulative deformation in the subsidence centers of the Nanpu development zone and Caofeidian new district during the heating season: (a) November 2018 to April 2019; (b) November 2019 to April 2020; (c) November 2020 to April 2021; and (d) November 2021 to April 2022.

dynamic water levels during water extraction and reinjection for heat exchange.

Referring to the pumping and recharging tests near the Caofeidian heating project (Fig. 10), following the onset of the heating seasons in November, the rapid decline in the flow rate of the extraction well [Fig. 10(c)] resulted in drainage consolidation of the strata, corresponding to the rapid subsidence in Stage I of Caofeidian new district (Fig. 11). Then the groundwater reinjection was carried out, and the groundwater flow in the extraction well was replenished [Fig. 10(a)]. At this point, the goal of achieving equilibrium in co-layered extraction and recharging technology was reached, ensuring the balance of the groundwater system in thermal reservoir. The stable dynamic water level alleviated the process of strata drainage consolidation, leading to the relief of subsidence deformation in Caofeidian new district, approaching a short-term stable state, corresponding to the end of Stage I and the beginning of Stage II (Fig. 11). After continuous groundwater reinjection for a period, the strata experienced replenishment rebound. At this point, the temporal deformation in Caofeidian new district even exhibited uplift, corresponding to the fluctuating deformation in Stage II (Fig. 11).

By February, there was an increased discrepancy in flow rate between water extraction and reinjection wells [Fig. 10(c)]. The continuous decline in the dynamic water level of the extraction well [Fig. 10(a)] initiated a new round of strata drainage consolidation. The subsidence deformation in Caofeidian new district further developed, corresponding to the end of Stage II, around April (Fig. 11). At this point, the limitations of colayered extraction and recharging technology became evident, as the disruption of the balance in the groundwater flow within the thermal reservoir contributed to the exacerbation of ground subsidence, restricting the sustainable utilization prospects of geothermal resources.

The cumulative subsidence amount in Nanpu development zone and Caofeidian new district for different months was statistically analyzed (Fig. 12). Combining the subsidence characteristics during the heating and rainy seasons, the subsidence mechanisms in these two areas can be summarized. Nanpu development zone, being an urban development area, currently lacks large-scale geothermal development. In winter, Nanpu development zone experienced a high demand for groundwater due to living needs, while precipitation was limited (Fig. 9). Continuous extraction of groundwater without natural replenishment led to sustained subsidence in Nanpu development zone (Fig. 12). During the rainy seasons, precipitation began to replenish groundwater, causing the strata to rebound, reversing the subsidence trend in Nanpu development zone and triggering uplift deformation (Fig. 12). Caofeidian new district is a newly developed urban area and an important geothermal field development area. In the early stages of heating, the demand for groundwater was high, and further extraction of groundwater for geothermal development accelerated the subsidence in Caofeidian new district (Fig. 12). The cumulative subsidence amount in Caofeidian new district was clearly larger than that in Nanpu development zone (Fig. 12). However, after the completion of geothermal exchange, artificial recharge of groundwater in Caofeidian new district mitigated the subsidence trend and even induced surface uplift. Therefore, during the heating season, Caofeidian new district exhibited alternating patterns of subsidence and uplift deformation (Fig. 12). After the heating season ended, the loss of groundwater due to geothermal development exacerbated the subsidence trend in Caofeidian new district, and some formations underwent irreversible plastic deformation. Even with precipitation replenishing groundwater during the rainy seasons, the rebound of the strata took longer, showing a lag compared to Nanpu development zone. Thus, the timing of uplift deformation in Caofeidian new district was approximately one month later than in Nanpu development zone (Fig. 12).

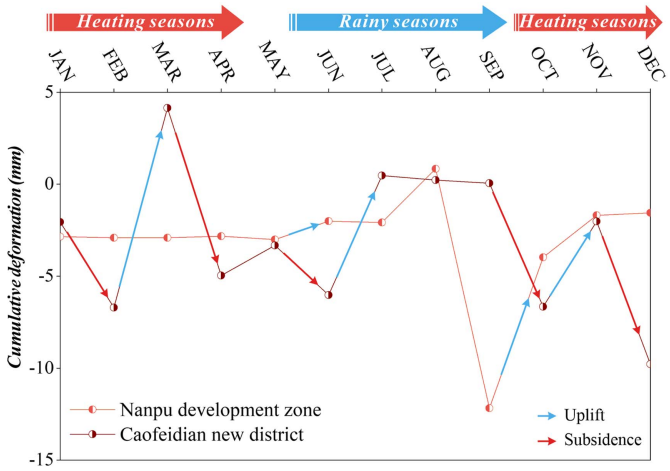

Fig. 12. Cumulative deformation in Nanpu development zone and Caofeidian new district during different months.

Environmental Effects and Potential Hazards Associated with Geothermal Field Subsidence

Ground subsidence is widespread worldwide, particularly prominent in newly-formed coastal areas. It often leads to extensive affected areas and severe economic losses (Wade et al. 2018). The serious consequences of ground subsidence encompass ground elevation loss, urban flooding, and structural damage (Huang and Jin 2018). Influenced by geothermal field development, Caofeidian new district experienced severe ground subsidence, posing a great threat to the economic and social development. Additionally, discrepancies in water extraction and reinjection volumes during geothermal field development would lead to the decline in dynamic water levels, accompanied by induced ground subsidence, which can trigger seawater intrusion (Gorelick and Zheng 2015; Loc et al. 2021). It impacts the sustainable development of thermal reservoir fluids, increases groundwater salinity, deteriorates the inland hydrogeological environment, and triggers a series of adverse environmental effects, including soil salinization. Salinization leads to soil compaction and fertility decline, affecting microbial and vegetation communities, further endangering the coastal ecosystem (Wang et al. 2023, 2024).

Prospects and Limitations of InSAR for Geothermal Reservoir Management

Sophisticated reservoir management is essential to avoid potential geological hazards induced by subsidence. For the future prospects of geothermal development in Caofeidian new district, it is essential to expedite the establishment of an effective reservoir management system taking advantage of on-site monitoring.

To circumvent the technological and financial challenges of monitoring the internal temperature and pressure of geothermal fluids, the focus can be shifted toward accurately capturing the large-scale deformation characteristics of geothermal field sites. Site deformation can serve as the initial displacement boundary condition for the geothermal reservoir model, enabling the inversion of internal fluid pressure (Geertsma et al. 1966; Geertsma 1973). Furthermore, by integrating thermal-fluid coupling models, real-time inversion of geothermal fluid temperature may be achievable

(Geertsma 1957). InSAR can provide high spatiotemporal density of geothermal site deformation, albeit susceptible to decorrelation factors (Tizzani et al. 2007). Therefore, it is necessary to complement InSAR with ground-based measurement techniques such as leveling and GPS measurements to establish precise deformation monitoring networks, addressing the accuracy limitation of SAR images. Additionally, there is a need to enhance the monitoring of dynamic water levels in extraction and reinjection wells, focusing on real-time changes in groundwater flow. The variation in water flow rates from geothermal production wells can assist in interpreting the deformation characteristics of the site. These measures are crucial for ground control and sustainable development of geothermal fields.

Conclusion

Geothermal energy is a breakthrough in the diversified development of traditional oilfield energy. However, during geothermal fluid extraction, changes in volume and pressure can lead to subsidence in the geothermal field, impacting its sustainable development, which needs to be controlled from a geothermal reservoir management perspective. Identifying ground subsidence caused by geothermal field development is crucial for the rational utilization of geothermal resources. This study focused on Caofeidian District, where Nanpu Oilfield is located, in North China. Using SBAS-InSAR technology, the ground surface deformation characteristics from October 2018 to May 2022 were inverted, identifying two subsidence centers: Nanpu development zone and Caofeidian new district. The maximum subsidence velocity in these two areas exceeded 50 mm/year. Since 2018, geothermal projects have been developed in the Caofeidian new district. There has been concentrated ground subsidence in the Caofeidian new district in April 2019, with a maximum cumulative subsidence exceeding 50 mm. By the end of May 2022, the maximum cumulative subsidence in the Caofeidian new district exceeded 150 mm.

As a note from reservoir management point of view, during the heating seasons, Caofeidian new district exhibited a phased pattern of rapid subsidence followed by uplift and alternating subsidence, while Nanpu development zone consistently maintained a subsidence trend. It was influenced by the fluctuations of flow rate in thermal reservoir during the geothermal development process. In November, there was a significant increase in water extraction for heat exchange, leading to a decline in the dynamic water level of the thermal reservoir. It resulted in drainage consolidation of the strata, and Caofeidian new district exhibited rapid subsidence. In April, there was discrepancy in flow rate between water extraction and reinjection wells. The decline in the dynamic water level of the thermal reservoir led to further drainage consolidation of the strata, exacerbating the ground subsidence trend in Caofeidian new district. During rainy seasons, despite water reinjection and groundwater replenishment from precipitation, the strata in the Caofeidian new district underwent irreversible plastic deformation, with a slow rebound process, lagging behind Nanpu development zone by one month. This paper revealed the subsidence mechanisms in the emerging coastal oilfield geothermal development zone and discussed the potential impacts of ground subsidence on the geological environment. In the future, it is imperative to further establish a sophisticated geothermal reservoir management system comprised of precise deformation monitoring networks, integrated with engineering geological and hydrogeological work, contributing to the prevention of geological and environmental disasters in geothermal fields.

Data Availability Statement

All data, models, and code generated or used during the study appear in the published article.

Acknowledgments

The first author Zhaoxi Wang would like to thank the support from State Scholarship Fund of China Scholarship Council (CSC NO. 202306170185). We express our sincere gratitude to the editors and all reviewers for their valuable and selfless reviews, which have significantly contributed to the enhancement of the manuscript.

References

Aydin, H., and S. Merey. 2021. "Potential of geothermal energy production from depleted gas fields: A case study of Dodan Field, Turkey." *Renewable Energy* 164 (Feb): 1076–1088. https://doi.org/10.1016/j.renene.2020.10.057.

Berardino, P., G. Fornaro, R. Lanari, and E. Sansosti. 2002. "A new algorithm for surface deformation monitoring based on small baseline differential SAR interferograms." *IEEE Trans. Geosci. Remote Sens.* 40 (11): 2375–2383. https://doi.org/10.1109/TGRS.2002.803792.

Bo, Q. Y., W. Q. Cheng, and T. Sun. 2021. "On the influencing mechanism of geothermal fluids on the dynamic changes of groundwater flow and heat transfer temperature." *Int. J. Heat Technol.* 39 (3): 992–1000. https://doi.org/10.18280/ijht.390337.

Cao, C., K. X. Zhu, T. H. Song, J. Bai, W. Zhang, J. P. Chen, and S. Y. Song. 2022a. "Comparative study on potential landslide identification with ALOS-2 and sentinel-1A data in Heavy Forest Reach, Upstream of the Jinsha River." *Remote Sens.* 14 (9). https://doi.org/10.3390/rs14091962.

Cao, C., K. X. Zhu, P. H. Xu, B. Shan, G. Yang, and S. Y. Song. 2022b. "Refined landslide susceptibility analysis based on InSAR technology and UAV multi-source data." *J. Cleaner Prod.* 368 (Sep): 133146. https://doi.org/10.1016/j.jclepro.2022.133146.

Chaussard, E., S. Wdowinski, E. Cabral-Cano, and F. Amelung. 2014. "Land subsidence in central Mexico detected by ALOS InSAR time-series." *Remote Sens. Environ.* 140 (Jan): 94–106. https://doi.org/10.1016/j.rse.2013.08.038.

Cigna, F., D. Tapete, V. H. Garduño-Monroy, J. A. Muñiz-Jauregui, O. H. García-Hernández, and A. Jiéenez-Haro. 2019. "Wide-area InSAR survey of surface deformation in urban areas and geothermal fields in the eastern trans-Mexican Volcanic Belt, Mexico." *Remote Sens.* 11 (20): 2341. https://doi.org/10.3390/rs11202341.

Dong, D. L., G. Lin, Y. F. F. Lin, M. D. Zhao, and K. Li. 2016. "Evaluating induced fractures between a large artificial lake and an aquifer-coal seam system: A case study in Tangshan Coal Mine, China." *Mine Water Environ.* 35 (2): 253–260. https://doi.org/10.1007/s10230-014-0319-z.

Dong, Y. X., H. X. Huang, L. Ren, H. D. Li, Z. Q. Du, E. Junjie, Q. Wang, and X. M. Zhang. 2021. "Geology and development of geothermal field in Neogene Guantao Formation in northern Bohai Bay Basin: A case of the Caofeidian geothermal heating project in Tangshan, China." *Pet. Explor. Dev.* 48 (3): 775–786. https://doi.org/10.1016/S1876-3804(21)60063-0.

Fibbi, G., T. Beni, R. Fanti, and M. Del Soldato. 2023. "Underground gas storage monitoring using free and open source InSAR data: A case study from Yela (Spain)." *Energies* 16 (17). https://doi.org/10.3390/en16176392.

García-Gil, A., J. Epting, C. Ayora, E. Garrido, E. Vázquez-Suñé, P. Huggenberger, and A. C. Gimenez. 2016. "A reactive transport model for the quantification of risks induced by groundwater heat pump systems in urban aquifers." *J. Hydrol.* 542 (Nov): 719–730. https://doi.org/10.1016/j.jhydrol.2016.09.042.

Geertsma, J. 1957. "A remark on the analogy between thermoelasticity and the elasticity of saturated porous media." *J. Mech. Phys. Solids* 6 (1): 13–16. https://doi.org/10.1016/0022-5096(57)90042-X.

Geertsma, J. 1966. "Problems of rock mechanics in petroleum production engineering." In *Proc., 1st ISRM Congress*. Lisbon, Portugal: Shell Internat Res Mij NV.

Geertsma, J. 1973. "A basic theory of subsidence due to reservoir compaction: The homogeneous case." *Verhandelingen Koninklijk Nederlands Geologisch en Mijnbouwkundig Genootschap* 23: 43–62.

Goldstein, R. M., and C. L. Werner. 1998. "Radar interferogram filtering for geophysical applications." *Geophys. Res. Lett.* 25 (21): 4035–4038. https://doi.org/10.1029/1998GL900033.

Gorelick, S. M., and C. M. Zheng. 2015. "Global change and the groundwater management challenge." *Water Resour. Res.* 51 (5): 3031–3051. https://doi.org/10.1002/2014WR016825.

Hoang, A. T., and V. Pham. 2021. "2-Methylfuran (MF) as a potential biofuel: A thorough review on the production pathway from biomass, combustion progress, and application in engines." *Renewable Sustainable Energy Rev.* 148 (Sep): 111265. https://doi.org/10.1016/j.rser.2021.111265.

Hoffmann, J., D. L. Galloway, and H. A. Zebker. 2003. "Inverse modeling of interbed storage parameters using land subsidence observations, Antelope Valley, California." *Water Resour. Res.* 39 (2). https://doi.org/10.1029/2001WR001252.

Hu, J., Q. J. Wang, Z. W. Li, R. Zhao, and Q. Sun. 2016. "Investigating the ground deformation and source model of the Yangbajing geothermal field in Tibet, China with the WLS InSAR Technique." *Remote Sens.* 8 (3): 191. https://doi.org/10.3390/rs8030191.

Huang, Y., and P. Jin. 2018. "Impact of human interventions on coastal and marine geological hazards: A review." *Bull. Eng. Geol. Environ.* 77 (3): 1081–1090. https://doi.org/10.1007/s10064-017-1089-1.

Janna, C., N. Castelletto, M. Ferronato, G. Gambolati, and P. Teatini. 2012. "A geomechanical transversely isotropic model of the Po River basin using PS InSAR derived horizontal displacement." *Int. J. Rock Mech. Min. Sci.* 51 (Apr): 105–118. https://doi.org/10.1016/j.ijrmms.2012.01.015.

Jiang, L. M., H. Lin, J. W. Ma, B. Kong, and Y. Wang. 2011. "Potential of small-baseline SAR interferometry for monitoring land subsidence related to underground coal fires: Wuda (Northern China) case study." *Remote Sens. Environ.* 115 (2): 257–268. https://doi.org/10.1016/j.rse.2010.08.008.

Karanam, V., M. Motagh, S. Garg, and K. Jain. 2021. "Multi-sensor remote sensing analysis of coal fire induced land subsidence in Jharia Coalfields, Jharkhand, India." *Int. J. Appl. Earth Obs. Geoinf.* 102 (Oct): 102439. https://doi.org/10.1016/j.jag.2021.102439.

Li, H. J. 2020. "Analysis and research on evolution characteristics and influencing factors of ground deformation in North China plain." Ph.D. thesis, Institute of Engineering Mechanics, China Earthquake Administration Harbin.

Li, X. Y., and Y. C. Li. 2023. "Study on land subsidence characteristics and deformation evolution mechanism in Caofeidian New Area, Bohai Bay." *Bull. Eng. Geol. Environ.* 82 (3): 1–12. https://doi.org/10.1007/s10064-023-03121-7.

Li, Y. J. 2013. "Study on the upper-crust electrical structure and its geological meaning in Tangshan-Qinghuangdao coastal region of Hebei province." Ph.D. thesis, Dept. of Geophysics, China Univ. of Geosciences (Beijing).

Liu, C. W., K. H. Lin, and Y. M. Kuo. 2003. "Application of factor analysis in the assessment of groundwater quality in a blackfoot disease area in Taiwan." *Sci. Total Environ.* 313 (1–3): 77–89. https://doi.org/10.1016/S0048-9697(02)00683-6.

Liu, F., P. C. Fu, R. J. Mellors, M. A. Plummer, S. T. Ali, E. C. Reinisch, Q. Liu, and K. L. Feigl. 2018. "Inferring geothermal reservoir processes at the raft river geothermal field, Idaho, USA, through modeling InSAR-measured surface deformation." *J. Geophys. Res. Solid Earth* 123 (5): 3645–3666. https://doi.org/10.1029/2017JB015223.

Liu, Y. L., H. J. Huang, Y. X. Liu, and H. B. Bi. 2016. "Linking land subsidence over the Yellow River delta, China, to hydrocarbon exploitation using multi-temporal InSAR." *Nat. Hazards* 84 (1): 271–291. https://doi.org/10.1007/s11069-016-2427-5.

Loc, H. H., D. V. Binh, E. Park, S. Shrestha, T. D. Dung, V. H. Son, N. H. T. Truc, N. P. Mai, and C. Seijger. 2021. "Intensifying saline water intrusion and drought in the Mekong Delta: From physical evidence to policy outlooks." *Sci. Total Environ.* 757 (Feb): 143919. https://doi.org/10.1016/j.scitotenv.2020.143919.

Maghsoudi, Y., F. van der Meer, C. Hecker, D. Perissin, and A. Saepuloh. 2018. "Using PS-InSAR to detect surface deformation in geothermal areas of West Java in Indonesia." *Int. J. Appl. Earth Obs. Geoinf.* 64 (Feb): 386–396. https://doi.org/10.1016/j.jag.2017.04.001.

Majorowicz, J., and M. Moore. 2014. "The feasibility and potential of geothermal heat in the deep Alberta foreland basin-Canada for CO_2 savings." *Renewable Energy* 66 (Jun): 541–549. https://doi.org/10.1016/j.renene.2013.12.044.

Nadeem, M., Z. L. Wang, and M. Shakeel. 2023. "Real output, fossil fuels, clean fuels and trade dynamics: New insights from structural break models in China." *Appl. Energy* 350 (Nov): 121746. https://doi.org/10.1016/j.apenergy.2023.121746.

Olah, G. A., G. K. S. Prakash, and A. Goeppert. 2011. "Anthropogenic chemical carbon cycle for a sustainable future." *J. Am. Chem. Soc.* 133 (33): 12881–12898. https://doi.org/10.1021/ja202642y.

Pirjola, L., et al. 2019. "Potential of renewable fuel to reduce diesel exhaust particle emissions." *Appl. Energy* 254 (Nov): 113636. https://doi.org/10.1016/j.apenergy.2019.113636.

Qin, X. Q., M. S. Liao, L. Zhang, and M. S. Yang. 2017. "Structural health and stability assessment of high-speed railways via thermal dilation mapping with time-series InSAR analysis." *IEEE J. Sel. Top. Appl. Earth Obs. Remote Sens.* 10 (6): 2999–3010. https://doi.org/10.1109/JSTARS.2017.2719025.

Qu, F. F., Z. Lu, Q. Zhang, G. W. Bawden, J. W. Kim, C. Y. Zhao, and W. Qu. 2015. "Mapping ground deformation over Houston-Galveston, Texas using multi-temporal InSAR." *Remote Sens. Environ.* 169 (Nov): 290–306. https://doi.org/10.1016/j.rse.2015.08.027.

Shen, S. L., H. N. Wu, Y. J. Cui, and Z. Y. Yin. 2014. "Long-term settlement behaviour of metro tunnels in the soft deposits of Shanghai." *Tunnelling Underground Space Technol.* 40 (Feb): 309–323. https://doi.org/10.1016/j.tust.2013.10.013.

Singleton, A., Z. Li, T. Hoey, and J. P. Muller. 2014. "Evaluating sub-pixel offset techniques as an alternative to D-InSAR for monitoring episodic landslide movements in vegetated terrain." *Remote Sens. Environ.* 147 (May): 133–144. https://doi.org/10.1016/j.rse.2014.03.003.

Suo, Z. Y., J. Q. Zhang, M. Li, Q. J. Zhang, and C. Fang. 2016. "Improved InSAR phase noise filter in frequency domain." *IEEE Trans. Geosci. Remote Sens.* 54 (2): 1185–1195. https://doi.org/10.1109/TGRS.2015.2476355.

Tizzani, P., P. Berardino, F. Casu, P. Euillades, M. Manzo, G. P. Ricciardi, G. Zeni, and R. Lanari. 2007. "Surface deformation of Long Valley Caldera and Mono Basin, California, investigated with the SBAS-InSAR approach." *Remote Sens. Environ.* 108 (3): 277–289. https://doi.org/10.1016/j.rse.2006.11.015.

Verdon, J. P., J. M. Kendall, A. L. Stork, R. A. Chadwick, D. J. White, and R. C. Bissell. 2013. "Comparison of geomechanical deformation induced by megatonne-scale CO_2 storage at Sleipner, Weyburn, and In Salah." *Proc. Natl. Acad. Sci. U S A* 110 (30): E2762–E2771. https://doi.org/10.1073/pnas.1302156110.

Wade, C. M., K. M. Cobourn, G. S. Amacher, and E. T. Hester. 2018. "Policy targeting to reduce economic damages from land subsidence." *Water Resour. Res.* 54 (7): 4401–4416. https://doi.org/10.1029/2017WR022133.

Wang, H. M., G. Q. Wang, J. C. Qi, H. Schandl, Y. M. Li, C. Y. Feng, X. C. Yang, Y. Wang, X. Z. Wang, and S. Liang. 2020. "Scarcity-weighted fossil fuel footprint of China at the provincial level." *Appl. Energy* 258 (Jan): 114081. https://doi.org/10.1016/j.apenergy.2019.114081.

Wang, S. F., Z. H. Pang, J. R. Liu, P. Lin, S. D. Liu, and M. Yin. 2013. "Origin and evolution characteristics of geothermal water in the niutuozhen geothermal field, North China Plain." *J. Earth Sci.* 24 (6): 891–902. https://doi.org/10.1007/s12583-013-0390-6.

Wang, Z., et al. 2023. "Integration of Sentinel–1 and Landsat–8 data for identifying deformation risk of hydraulic engineering in seasonally frozen salinization regions." *CATENA* 233 (Dec): 107477. https://doi.org/10.1016/j.catena.2023.107477.

Wang, Z. X., et al. 2024. "Multi-scale failure mechanisms of hydraulic engineering exposed to seasonally frozen salinization environment: Integrating SBAS-InSAR and mechanical experiments." *Sci. Total*

Environ. 912 (Feb): 169210. https://doi.org/10.1016/j.scitotenv.2023.169210.

Wei, F. H. 2006. Researches on geological hazard and risk zonation in Tangshan." Ph.D. thesis, Dept. of Geological Engineering, China Univ. of Geosciences (Beijing).

Yang, Q., W. L. Zhao, T. H. Dixon, F. Amelung, W. S. Han, and P. Li. 2015. "InSAR monitoring of ground deformation due to CO_2 injection at an enhanced oil recovery site, West Texas." *Int. J. Greenhouse Gas Control* 41 (Oct): 20–28. https://doi.org/10.1016/j.ijggc.2015.06.016.

Yi, Z., M. Xingmin, N. Allesandro, D. Tom, C. Guan, J. Colm, L. Yuanxi, and S. Xiaojun. 2022. "Characterization of pre-failure deformation and evolution of a large earthflow using InSAR monitoring and optical image interpretation." *Landslides* 19 (1): 35–50. https://doi.org/10.1007/s10346-021-01744-z.

Yu, Q. B., Q. Wang, X. X. Yan, T. L. Yang, S. Y. Song, M. Yao, K. Zhou, and X. L. Huang. 2020a. "Ground deformation of the Chongming east shoal reclamation area in Shanghai based on SBAS-InSAR and laboratory tests." *Remote Sens.* 12 (6): 1016. https://doi.org/10.3390/rs12061016.

Yu, Q. B., X. X. Yan, Q. Wang, T. L. Yang, Y. Y. Kong, X. L. Huang, and Q. Mehmood. 2020b. "X-ray computed tomography-based evaluation of the physical properties and compressibility of soil in a reclamation area." *Geoderma* 375 (Oct): 114524. https://doi.org/10.1016/j.geoderma.2020.114524.